BALLISTIC PERFORMANCE OF ALUMINA/S-2 GLASS-REINFORCED POLYMER-MATRIX COMPOSITE HYBRID LIGHTWEIGHT ARMOR AGAINST ARMOR PIERCING (AP) AND NON-AP PROJECTILES

M. Grujicic[1*], B. Pandurangan[1], U. Zecevic[1], K. L. Koudela[2], B. A. Cheeseman[3]

[1] *Department of Mechanical Engineering Clemson University, Clemson SC 29634*

[2] *Applied Research Laboratory, Pennsylvania State University 155, ARL Building, University Park, PA 16802*

[3] *Army Research Laboratory – Survivability Materials BranchAberdeen, Proving Ground, MD 21005-5069*

Abstract—The ability of light-weight all fiber-reinforced polymer-matrix composite armor and hybrid composite-based armor hard-faced with ceramic tiles to withstand the impact of a non-Armor-Piercing (non-AP) and AP projectiles is investigated using a transient non-linear dynamics computational analysis. The results obtained confirm experimental findings that the all-composite armor, while being able to successfully defeat non-AP threats, provides very little protection against AP projectiles. In the case of the hybrid armor, it is found that, at a fixed overall areal density of the armor, there is an optimal ratio of the ceramic-to-composite areal densities which is associated with a maximum ballistic armor performance against AP threats.

  The results obtained are rationalized using an analysis based on the shock/blast wave reflection and transmission behavior at the hard-face/air, hard-face/backing and backing/air interfaces, projectiles' wear and erosion and the intrinsic properties of the constituent materials of the armor and the projectiles.

NOMENCLATURE

A	-	Material Specific Constant in JH2 Strength Model
A_1	-	Room temperature yield stress of AISI 4340 Steel
a	-	Material Parameter in Yield Function for the Composite Laminate
B	-	Material Specific Constant in JH2 Strength Model
B_1	-	Strain Hardening Constant of AISI 4340 Steel
β	-	Fraction of Internal Elastic Energy converted to Potential Energy

* E-mail: mica.grujicic@ces.clemson.edu
  Tel: (864) 656-5639, Fax: (864) 656-4435

Report Documentation Page

Public reporting burden for the collection of information is estimated to average 1 hour per response, including the time for reviewing instructions, searching existing data sources, gathering and maintaining the data needed, and completing and reviewing the collection of information. Send comments regarding this burden estimate or any other aspect of this collection of information, including suggestions for reducing this burden, to Washington Headquarters Services, Directorate for Information Operations and Reports, 1215 Jefferson Davis Highway, Suite 1204, Arlington VA 22202-4302. Respondents should be aware that notwithstanding any other provision of law, no person shall be subject to a penalty for failing to comply with a collection of information if it does not display a currently valid OMB control number.

1. REPORT DATE **2007**	2. REPORT TYPE	3. DATES COVERED **00-00-2007 to 00-00-2007**

4. TITLE AND SUBTITLE	5a. CONTRACT NUMBER
Ballistic Performance of Alimina/S-2 Glass-Reinforced Polymer-Matrix Composite Hybrid Lightweight Armor Against Armor Piercing (AP) and Non-AP Projectiles	5b. GRANT NUMBER
	5c. PROGRAM ELEMENT NUMBER
6. AUTHOR(S)	5d. PROJECT NUMBER
	5e. TASK NUMBER
	5f. WORK UNIT NUMBER

7. PERFORMING ORGANIZATION NAME(S) AND ADDRESS(ES) **Celmson University,Department of Mechanical Engineering,Clemson,SC,29634**	8. PERFORMING ORGANIZATION REPORT NUMBER

9. SPONSORING/MONITORING AGENCY NAME(S) AND ADDRESS(ES)	10. SPONSOR/MONITOR'S ACRONYM(S)
	11. SPONSOR/MONITOR'S REPORT NUMBER(S)

12. DISTRIBUTION/AVAILABILITY STATEMENT
Approved for public release; distribution unlimited

13. SUPPLEMENTARY NOTES
Multidiscipline Modeling in Materials and Structures, 3, pp. 287-312, 2007

14. ABSTRACT

The ability of light-weight all fiber-reinforced polymer-matrix composite armor and hybrid composite-based armor hard-faced with ceramic tiles to withstand the impact of a non-Armor- Piercing (non-AP) and AP projectiles is investigated using a transient non-linear dynamics computational analysis. The results obtained confirm experimental findings that the all-composite armor, while being able to successfully defeat non-AP threats, provides very little protection against AP projectiles. In the case of the hybrid armor, it is found that, at a fixed overall areal density of the armor there is an optimal ratio of the ceramic-to-composite areal densities which is associated with a maximum ballistic armor performance against AP threats. The results obtained are rationalized using an analysis based on the shock/blast wave reflection and transmission behavior at the hard-face/air, hard-face/backing and backing/air interfaces, projectiles? wear and erosion and the intrinsic properties of the constituent materials of the armor and the projectiles.

15. SUBJECT TERMS

16. SECURITY CLASSIFICATION OF:			17. LIMITATION OF ABSTRACT	18. NUMBER OF PAGES	19a. NAME OF RESPONSIBLE PERSON
a. REPORT **unclassified**	b. ABSTRACT **unclassified**	c. THIS PAGE **unclassified**	**Same as Report (SAR)**	**28**	

c	-	Elastic Constant of a Lamina in the Composite Laminate
$\bar{c}$	-	Effective Elastic Constant of the Composite Laminate
C	-	Material Specific Constant in JH2 Strength Model
C_1	-	Strain rate constant for the AISI 4340 Steel
D	-	Damage Parameter
D_3-D_7	-	Material Specific Constant in JH2 Strength Model
$d\lambda$	-	Plastic Strain Rate Multiplier
e	-	Internal energy
E	-	Young's Modulus
ε	-	Plastic strain
G	-	Shear modulus
Γ	-	Gruneisen parameter
K	-	Bulk Modulus
K_1-K_3	-	Constants in Polynomial Equation of State
υ	-	Volume fraction of the fibers in the Composite Laminate
μ	-	Compressibility Factor
v	-	Poisson's Ratio
P	-	Pressure
R	-	Parameter quantifying resistance of the material to plastic deformation
ρ	-	Density
σ	-	Stress
σ^*	-	Normalized Yield Strength
T	-	Temperature
t	-	Time
U	-	Internal Elastic Energy
v	-	Specific volume

Subscripts

o	-	Initial condition
H	-	Hugoniot quantity
HEL	-	Hugoniot Elastic Limit
H_0	-	Homologous quantity
i, j	-	Directional Indices
$melt$	-	Melting point quantity
pl	-	Plastic state quantity
$room$	-	Room temperature quantity
vol	-	Volumetric quantity

Superscripts

d	-	Deviatoric quantity
M	-	Material Specific Parameter in JH2 Strength Model
N	-	Material Specific Parameter in JH2 Strength Model
m	-	Thermal softening exponent
n	-	Strain hardening exponent

1. Introduction

Due to their high strength and stiffness to weight ratios, polymer-matrix composites are increasingly being used in the construction of rapidly deployable armored vehicles. Polymer-matrix composites have also become quite popular as lightweight armor. This is particularly evidenced in the case of the M1114 High Mobility Multi-Purpose Wheeled Vehicles (more commonly referred to as the Humvee) in which the armor is typically made of HJ1 composite material. This patented, licensed composite material system complies with the MIL-L-64154 U.S. Military Department of Defense Specifications [1] and is comprised of high-strength S-2 glass-fiber reinforcements and a phenolic-resin based polymeric matrix. Such armor panels offer superior protection against fragmented ballistic threats when compared to monolithic armor panels on an equivalent weight basis, but little protection against Armour Piercing (AP) threats [2].

AP ammunition is specially designed to defeat the hardened armor of modern military vehicles. It is typically comprised of a sharp and hard penetrator (generally made of hardened steel or tungsten) which is surrounded by a guilding metal jacket. When an AP projectile hits armor, the guilding metal jacket becomes rapidly and severely deformed and drops away, leaving the sharp penetrator to bore its way through the armor at a high velocity. Due to their relatively low (absolute) hardness, fiber-reinforced composite armors are unable to blunt the hard tip of the penetrator, offering very little protection. This shortcoming is typically mitigated through the addition of a hardened face to the outer surface of the armor. The addition of the hardened face helps blunt the projectile and limits its ability to focus the kinetic energy it carries to the pointed tip.

The design of a single-material armor system to defeat a given threat level is typically done using the following procedure: (a) A number of armor panels with different areal densities (the weight per unit area) are tested against the projectiles at varying velocities; (b) For each case, the velocity (generally referred to as V50) is determined at which the probability for the armor penetration is 50%; (c) A plot of areal density vs. V50 is next constructed, and the areal density at which the V50 equals the expected impact velocity of the incoming threat is interpolated; (d) The result obtained in (c) is verified with further testing; and (e) Finally, a safety factor is added to make the armor penetration probability exceptionally and acceptably low. In the case of an armor consisting of a ceramic face and a fiber-reinforced polymer-matrix composite backing, in addition to the areal density the ratio of ceramic areal density to composite areal density must also be considered in the design of the armor [2].

The ballistic performance of the S-2 glass fiber-reinforcement polymer-matrix composite armor panels has been the subject of an intense study in the past two decades [3,4 and 5]. The main results of the study can be summarized as follows: (a) Compared to the more common E-glass fibers, S-2 glass fibers possess a higher strength and elongation and, thus, a substantially higher energy absorbing potential; (b) the total energy dissipation potential of the composite armor panels reinforced with the S-2 glass fibers is the sum of the armor strain energy and kinetic energy, both of which increase linearly with an increase in the areal density of the armor; (c) a linear relationship exists between the V50 and the areal density divided by panel thickness suggesting that the armor resistance to penetration is proportional to the number of fibers intersected by the projectile and (d) the energy absorbed by the armor is strongly affected by the nose shape of the projectile. Blunt projectiles are found to be promptly and significantly decelerated by the initial, intense impact shock waves. Furthermore, blunt projectiles were less effective at penetrating the armor because they had to cut the encountered

fibers at two places and to accelerate the material in front of the projectile in the rearward direction. On the other hand, sharp-nosed projectiles were observed to push the fibers away in the lateral directions, causing the fibers around the penetration cavities to kink (buckle). Fiber buckling, being a localized deformation process, is generally associated with little energy absorption.

The findings reported above can be used to explain why armor-piercing projectiles are so effective against all fiber-reinforced polymer-matrix composite armor like HJ1: that is, neither the fibers nor the matrix of the composite material are hard enough to cause blunting of the AP projectile's sharp, hardened penetrator nose. The same 100% HJ1-composite armor, on the other hand, is quite effective in defeating non-AP threats. This is clearly demonstrated in Fig.1 in which a plot is given of the V50 as a function of the areal density for the all HJ1 composite armor against a non-AP threat (a .30 caliber M80 full metal jacketed, FMJ, projectile) [8]. A single data point is shown for the same armor tested against a .30 caliber M2 AP projectile. It is evident that the HJ1 armor is quite effective at stopping the non-AP threat; but ineffective against AP threats. As discussed earlier, one solution to defeating the AP projectiles that has been successfully implemented is to apply ceramic tiles (which are light, hard, and strong in compression) to the outer surface of the composite armor. In the resulting hybrid armor system, each material plays a specific role. During a ballistic impact, ceramic tiles experience high compressive forces. Yet, ceramics are extremely strong in compression and typically will not immediately fail. During the early stage of impact, high hardness of the ceramic will cause erosion of the projectile tip. This is followed by (tensile) failure of the ceramic as the compressive shock wave upon reaching the back surface of the tile is reflected as a tensile wave [7]. By that time, however, the ceramic has absorbed some projectile's kinetic energy and, more importantly, has succeeded in eroding the tip of the projectile. Consequently, the eroded projectile becomes less efficient in pushing aside the fibers as it enters the HJ1 composite backing of the hybrid armor. The composite backing serves a dual purpose: (i) it carries the bulk of the structural loads and (ii) it also absorbs the kinetic energy of the eroded AP projectile. This kinetic energy absorption takes place through a combination of mechanisms such as fiber deformation and fracture, fiber pullout, and composite delamination.

As pointed out earlier, the ratio of composite backing to ceramic facing areal densities at a fixed overall areal density is an important design parameter in hybrid armor. In a recent work, Fecko et al. [2] tested the ballistic performance of several HJ1-based hybrid armor panels hard-faced with Al_2O_3 ceramic tiles, all with a fixed total areal density of $51kg/m^2$ against the .30 caliber M2 AP projectile. The results obtained (Fig.2) show that there is an optimal HJ1-composite content (defined as the percent of total areal density allotted to the HJ1), located between 0 and 40% at which the ballistic performance of the hybrid armor is maximized. Furthermore, at HJ1 contents above 40%, the V50 decreases linearly with an increase in the HJ1 content.

The main objective of the present work is to carry out a detailed computational analysis of the ballistic performance of the all HJ1-composite and the HJ1-based hybrid armor panels hard-faced with Al_2O_3 ceramic tiles with respect to .30 caliber M80 FMJ non-AP and M2 AP projectiles in order to better understand the role the ceramic-to-polymer areal density ratio plays in defeating such threats.

The organization of the paper is as follows. A brief overview of the non-linear dynamics computational procedure utilized in the present work is given in Section 2.1.

Constitutive models used to represent the behavior of the projectiles and armor materials under ballistic impact conditions are discussed in Section 2.2. Details of the numerical model used to analyze the impact and penetration of the armor by the non-AP and AP projectiles are presented in Section 2.3. The results obtained in the current work are presented and discussed in Section 3. The main conclusions resulting from the present work are summarized in Section 4.
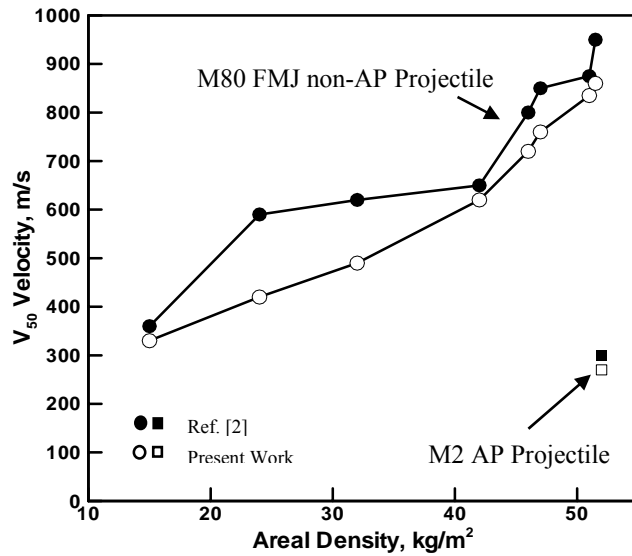
Fig.1. Ballistic Performance of all HJ1 Composite Armor Impacted with Non-Armor Piercing and 0.3 Caliber APM2 Armor Piercing Projectiles
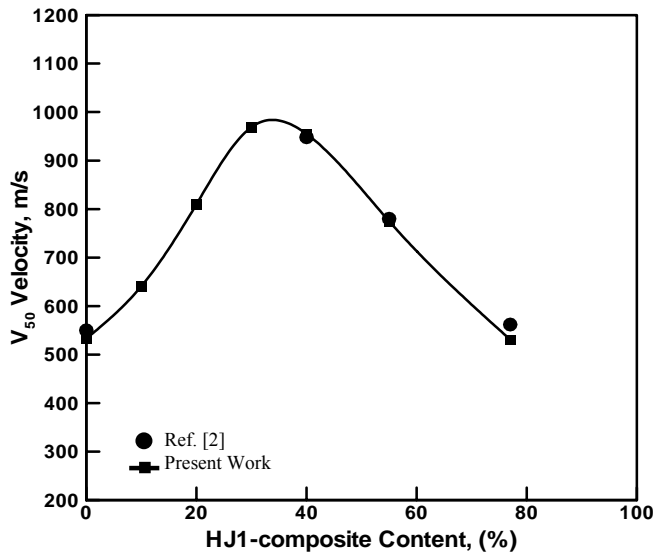
Fig.2. The effect of the HJ1-composite content (percent of areal density) on the Ballistic Performance of Alumina/HJ1Ceramic/Composite Hybrid Armor impacted with 0.3 Caliber APM2 projectiles.

2. COMPUTATIONAL PROCEDURE

2.1. Non-linear Dynamics Modeling of High-rate Phenomena

All the calculations carried out in the present work are done using AUTODYN, a general purpose non-linear dynamics modeling and simulation software [8]. AUTODYN falls into a group of computer programs known as "*hydrocodes*", which are particularly suited for modeling explosion, blast, impact and penetration events. Within the code, the appropriate mass, momentum and energy conservation equations coupled with the materials modeling equations and subjected to the appropriate initial and boundary conditions are solved. These equations are solved using different numerical methods and the choice of the method ("*processor*") is driven by the physical nature of the problem. Lagrange processor is typically used for solid continuum and structures) and the Euler processor is commonly used for modeling gases, liquids or solids subject to large deformations. Solid continuum and structures are also analyzed using the gridless SPH (Smooth Particle Hydrodynamics) processor which does not suffer from a grid tangling problem (typically encountered in Lagrange processor) and does not entail the use of an unphysical erosion algorithm (removal of highly distorted grids to help the numerical procedure).

In the present work, the ballistic performance of the armor under non-AP and AP threats is analyzed using the Lagrange and SPH processors. The interactions between different sub-domains are accounted for through the use of the sub-domain interaction options within AUTODYN [8]. A detailed overview of the sub-domain interaction options can be found in our recent work [9].

2.2. Materials Constitutive Models

As discussed in the previous section, for the boundary value problems analyzed by AUTODYN to be fully specified, material-specific constitutive relations involving the flow variables (pressure, mass density, internal energy density, temperature, etc.) have to be defined. These additional relations typically involve an equation of state, a strength equation and a failure equation for each constituent material. These equations arise from the fact that, in general, the total stress tensor can be decomposed into a sum of a hydrostatic stress (pressure) tensor (which causes a change in the volume/density of the material) and a deviatoric stress tensor (which is responsible for the shape change of the material). An equation of state then is used to define the corresponding functional relationship between pressure, mass-density (specific volume) and internal energy density (temperature), while a strength relation is used to define the appropriate equivalent plastic-strain, equivalent plastic-strain rate, and temperature dependencies of the yield surface (a scalar function of the deviatoric stress or total stress components). In addition, a material model generally includes a failure criterion, i.e. an equation describing the (hydrostatic or deviatoric) stress and/or strain condition which, when attained, causes the material to fracture and lose (abruptly, in the case of brittle materials or gradually, in the case of ductile materials) its ability to support normal and shear stresses.

In the following, a brief description is given of the models for the materials utilized in the present work, i.e. for fiber-reinforced polymer-matrix composite HJ1 laminate (armor backing), alumina (hard-face of the armor) and the metallic materials (lead,

tungsten and copper) used in the construction of the non-AP and AP projectiles. The values of all the material parameters defined in the remainder of the section are available in the AUTODYN materials library [8] and, hence can be accessed by all licensed AUTODYN users.

2.2.1 Fiber-reinforced Polymer-matrix Composite Laminates

The mechanical behavior of composite laminates is generally more complex than that found in metals or ceramics. As discussed in our previous work [9], this increased complexity of the composite laminates can be attributed to a number of phenomena, such as: (a) anisotropy of the material stiffness properties; (b) anisotropy in the failure strength and in the post-failure behavior; (c) coupling between the hydrostatic and deviatoric (stress and strain) quantities; (d) non-linearity in pressure vs. density relation; and (e) onset of compaction when the material contains porosity.

In the present work, the mechanical responses of the composite laminates under large deformation and high deformation-rate conditions (which are encountered during ballistic testing) are represented using the ballistic orthotropic material model developed by Clegg et al. [10]. This model is based on the original ideas proposed by Anderson et al. [11] for coupling the material's anisotropy with the non-linear material response. Since this model was reviewed in details in our recent work [12], it will be only summarized here.

Unlike metals and ceramics that have nearly identical properties in all directions and are, hence, referred to as "isotropic" materials, composite laminates possess properties which may be very different in a direction parallel with the laminate plane and in the through-the-thickness direction. A composite armor panel is typically constructed by laminating few dozens of individual plies (laminas) so that the overall in-plane properties of the laminate are isotropic. Therefore, composite laminates are classified as "*transversely isotropic*" materials. The linear elastic stiffness matrix in such materials involves six independent elastic constants, and is represented as:

$$
\begin{bmatrix} \sigma_1 \\ \sigma_2 \\ \sigma_3 \\ \sigma_{23} \\ \sigma_{31} \\ \sigma_{12} \end{bmatrix} =
\begin{bmatrix}
c_{11} & c_{11} & c_{13} & 0 & 0 & 0 \\
c_{11} & c_{11} & c_{13} & 0 & 0 & 0 \\
c_{13} & c_{13} & c_{33} & 0 & 0 & 0 \\
0 & 0 & 0 & c_{44} & 0 & 0 \\
0 & 0 & 0 & 0 & c_{55} & 0 \\
0 & 0 & 0 & 0 & 0 & c_{66}
\end{bmatrix}
\begin{bmatrix} \varepsilon_1 \\ \varepsilon_2 \\ \varepsilon_3 \\ \varepsilon_{23} \\ \varepsilon_{31} \\ \varepsilon_{12} \end{bmatrix}
\tag{1}
$$

where σ_{ij}, ε_{ij} and c_{ij} are elements of the stress, strain and stiffness matrix, respectively. Following the AUTODYN convention in Eq. (1), the "*principal*" direction 3 is taken to coincide with the through-the-thickness direction while principal directions 1 and 2 are in-plane directions. It should be noted that in the current formulation of the composite material models used in AUTODYN, the effect of thermal strains is not considered. In addition, a local adiabatic condition is assumed. In other words, no consideration is given to thermal conduction.

The values of the transversely-isotropic linear elastic constants given in Eq. (1), c_{ij},

can be computed using the Young's moduli in the principal material directions, E_{ii}, $i=1,2,3$, shear moduli, G_{ij} (associated with shear on a principal plane i, in a principal direction j), Poison's ratio, v_{ij} (defined as the negative ratio of transverse strain in the j direction and longitudinal strain in the i direction, i.e., $v_{ij} = -\dfrac{\varepsilon_j}{\varepsilon_i}$). The appropriate relationships needed to compute the transversely-isotropic linear elastic constants can be found in our recent work [12]. The values of the elastic constants (E_{ii}, G_{ij}, v_{ij}) are obtained using a series of mechanical tests as described in Table 1.

Table1. Mechanical Tests and Analytical Relations used for Determination of the Various Mechanical Properties of Orthotropic Composite Laminates

Material Property	Evaluation Procedure
Young's Modulus along through-the-thickness direction E_{11}	Estimated from Inverse Flyer Plate Tests and other relations e.g. $v_{12}/E_{11} = v_{21}/E_{22}$
In-plane Young's Modulus E_{22}	Calculated from $0°$ Tension tests
In-plane Young's Modulus E_{33}	Calculated from $90°$ Tension tests
In-plane Poisson's Ratio v_{23}	Calculated from $0°$ Tension tests using strain gages in 22 and 33 directions
Out-of-plane Poisson's Ratio v_{31}	Calculated from $90°$ Tension tests using strain gages in 11 and 33 directions
Out-of-plane Poisson's Ratio v_{12}	Calculated from $0°$ Tension tests using strain gages in 11 and 22 directions and using $v_{12}/E_{11} = v_{21}/E_{22.}$ (E_{11} known)
In-plane Shear Modulus G_{23}	Calculated from $45°$ Tension tests
Out-of-plane Shear Modulus G_{31}	Calculated from short beam shear tests
Out-of-plane Shear Modulus G_{12}	Calculated from short beam shear tests

Equation of State

Using the definition of the volumetric strain $\varepsilon_{vol} = \varepsilon_{11} + \varepsilon_{22} + \varepsilon_{33}$ and Eq. (1), the linear elastic stress-strain relation for a transversely-isotropic material can be written as:

$$
\begin{bmatrix} \sigma_{11} \\ \sigma_{22} \\ \sigma_{33} \\ \sigma_{23} \\ \sigma_{31} \\ \sigma_{12} \end{bmatrix} = \begin{bmatrix} c_{11} & c_{11} & c_{13} & 0 & 0 & 0 \\ c_{11} & c_{11} & c_{13} & 0 & 0 & 0 \\ c_{13} & c_{13} & c_{33} & 0 & 0 & 0 \\ 0 & 0 & 0 & c_{44} & 0 & 0 \\ 0 & 0 & 0 & 0 & c_{55} & 0 \\ 0 & 0 & 0 & 0 & 0 & c_{66} \end{bmatrix} \begin{bmatrix} \frac{1}{3}\varepsilon_{vol} + \varepsilon_{11}^d \\ \frac{1}{3}\varepsilon_{vol} + \varepsilon_{22}^d \\ \frac{1}{3}\varepsilon_{vol} + \varepsilon_{33}^d \\ \varepsilon_{23}^d \\ \varepsilon_{31}^d \\ \varepsilon_{12}^d \end{bmatrix}
\tag{2}
$$

where ε_{ij}^d are the components of the deviatoric strain. Furthermore, using the definition

of pressure $P = -\frac{1}{3}(\sigma_{11} + \sigma_{22} + \sigma_{33})$ and Eq. (2) the following relation can be

obtained:

$$
P = -\frac{1}{9}\left[\bar{c}_{11} + \bar{c}_{11} + \bar{c}_{33} + 2(\bar{c}_{11} + \bar{c}_{13} + \bar{c}_{13})\right]\varepsilon_{vol} - \frac{1}{3}(\bar{c}_{11} + \bar{c}_{11} + \bar{c}_{13})\varepsilon_{11}^d - \frac{1}{3}(\bar{c}_{11} + \bar{c}_{11} + \bar{c}_{13})\varepsilon_{22}^d -
$$
$$
-\frac{1}{3}(\bar{c}_{13} + \bar{c}_{13} + \bar{c}_{33})\varepsilon_{33}^d - (\bar{c}_{16} + \bar{c}_{26} + \bar{c}_{36})\varepsilon_{11}^d
\tag{3}
$$

The first term on the right hand side of Eq. (3) represents the standard linear relationship between the pressure and volumetric strain while the remaining terms on the right hand side of the same equation account for the coupling between the pressure and the deviatoric strain. The later terms of Eq. (3) are absent in the case of isotropic materials. The constant part of the first term on the right hand side of Eq. (3) represents the effective bulk modulus of the material, K. Under high strain-rate ballistic loading conditions, the relationship between the pressure and the volumetric strain is typically non-linear and, consequently, the first term on the right hand side of Eq. (3) is replaced by a non-linear relationship between the pressure and volumetric strain. Usually, the Mie-Gruneisen [13] equation of state is used to represent the first term on the right hand side of Eq. (3).

The Mie-Gruneisen equation of state defines the effect of current material mass density, ρ, and internal energy density, e, on pressure, P, as:

$$
P = P_H + \Gamma\rho[e - e_H]
\tag{4}
$$

where P_H and e_H represent respectively the pressure and the internal energy density associated with the Hugoniot shock states of the material. These reference states are obtained by solving a system of simultaneous algebraic equations defining, for a stationary shock, the mass conservation, the momentum conservation and the energy conservation and a linear relationship between the shock speed, us and the particle velocity u_p. The parameter Γ appearing in Eq. (4) (the Gruneisen Gamma) is a known

thermodynamic material property and is defined as: $\Gamma(\rho) \equiv \frac{1}{\rho}\left(\frac{\partial P}{\partial e}\right)_{\frac{1}{\rho}}$. Gruneisen

Gamma allows the determination of thermodynamic states away from the reference

Hugoniot states.

Strength Model

The strength model for transversely-isotropic materials is typically represented using the following type of total-stress based nine-parameter quadratic yield function:

$$
\begin{aligned}
f(\sigma_{ij}) = a_{11}\sigma_{11}^2 + a_{22}\sigma_{22}^2 + a_{33}\sigma_{33}^2 + 2a_{12}\sigma_{11}\sigma_{22} + 2a_{23}\sigma_{22}\sigma_{33} + 2a_{13}\sigma_{11}\sigma_{33} + \\
+ 2a_{44}\sigma_{23}^2 + 2a_{55}\sigma_{31}^2 + 2a_{66}\sigma_{12}^2 = R
\end{aligned}
\tag{5}
$$

where a_{ij} and R are material parameters. The parameter R represents the current material's resistance towards plastic deformation and in the case of strain-hardening materials like composite laminates increases with an increase in the equivalent plastic strain.

Equation (5) is used in the following fashion: When $f(\sigma_{ij})$ defined in Eq. (5) is less than R, no plastic deformation takes place, otherwise, plasticity takes place and the R parameter is increased until the equality defined by Eq. (5) is satisfied. Plastic deformation in composite laminates is assumed to take place in accordance with the associated flow rule, i.e. the magnitude of the components of the plastic strain increment scale linearly with the associated components of the stress gradient of the yield function as:

$$
d\varepsilon_{ij}^p = d\lambda \frac{\partial f}{\partial \sigma_{ij}}
\tag{6}
$$

where $d\lambda$ is the plastic strain-rate multiplier.

Failure Model

The failure model for transversely-isotropic composite laminates used in the present work combines a failure initiation model with a material mechanical degradation model. Final failure is taken to occur when the material loses its ability to support any shear and/or tensile loads. The failure initiation model defines a stress or strain based criterion which, when met, leads to the onset of mechanical degradation of the material. Once failure is initiated, the strength and stiffness properties of the material are continuously updated in accordance with the extent of current level of material degradation. The material mechanical degradation model is based on the concept of cracked strain, ε_{cr}, which gives rise to a progressive increase in the extent of material damage as it increases from the moment of failure initiation. The maximum value of each component of cracked strain is obtained using the computed or measured values of the associated failure stress and fracture energy. The fracture energies are determined experimentally using the double cantilever beam test [14].

Once the material has failed in a particular direction, the stress in that direction is set to zero while the stresses in the other directions are modified in accordance with the loss of Poisson's effect. When the failure occurs due to excessive tensile strains in the laminate through-thickness direction or due to excessive inter-lamellar shear strains, it is referred to as "*delamination*". On the other hand, laminate in-plane tensile stresses lead to "*reinforcement*" failure. When the material fails in more than one direction (*the bulk failure*) its properties are set to those of an equivalent isotropic material, and all tensile

stresses are set to zero, while the shear stresses are set to a predefined residual shear stress level.

In addition to the stress/strain based failure criterion described above, matrix melting and/or fiber degradation due to excessive heating can also lead to material failure. Matrix melting occurs when the temperature exceeds the melting point of the polymer matrix and results in delamination failure mode. Fiber degradation occurs when the matrix temperature exceeds a predefined fiber degradation temperature and leads to a bulk mode of failure which leaves the material only with an ability to support compressive type of stresses. In the present formulation of the composite-material degradation and failure model, the effect of thermal strains is not considered.

Erosion Model

When the Lagrange solver is used for computations, numerical difficulties arising from excessive distortion of the cells are often overcome by using an erosion algorithm, which at a predefined level of equivalent geometrical or plastic strain removes excessively distorted cells while transferring the momentum associated with the removed nodes to the remaining nodes. For composite laminates, the erosion criterion is typically defined using a value of 1-2 for the instantaneous geometrical strain since this range of erosion strains appear to give the best agreement between the computational and experimental results.

2.2.2 Alumina/Structural Ceramic Materials

Equation of State

For structural ceramics like alumina, the polynomial equation of state is most frequently used within which the relationship between pressure, mass density and internal energy density in a damage-free ceramic is defined as:

$$P = K_1\mu + K_2\mu^2 + K_3\mu^3, \ \ \mu > 0 \tag{7}$$

and

$$P = K_1\mu, \ \ \mu < 0 \tag{8}$$

where $\mu = (\rho/\rho_0 - 1)$, ρ_0 the reference density, K_1 is the bulk modulus of the material and K_2 and K_3 are higher-order bulk modulii.

In ceramics with a non-zero extent of damage, $D>0$), the equation of state is modified to include the effects of bulking. Bulking is a phenomenon occurring in brittle materials like ceramics during fracture in where there is an increase in the material volume (i.e. a decrease in the mass density of the material) at a constant pressure or alternatively an increase in pressure at a constant mass density of the material. The bulking modified equation of state is then given by [8]:

$$P = K_1\mu + K_2\mu^2 + K_3\mu^3 + \Delta P, \ \ \mu > 0 \tag{9}$$

where the bulking-induced pressure increment, ΔP, is determined from energy considerations and varies from zero at $D=0$ to ΔP_{max} at $D=1.0$. Assuming that the fraction of the internal elastic energy decrease arising from the decrease in deviatoric stresses in the ceramic is converted to an increase in potential internal energy, the incremental pressure term ΔP at a time $t + \Delta t$ can be represented in terms of ΔP at the

time t as:

$$\Delta P(t+\Delta t) = -K\mu(t+\Delta t) + \sqrt{(K_1\mu(t+\Delta t) + \Delta P(t))^2 + 2\beta K_1 \Delta U}, \quad \mu(t+\Delta t) \quad (10)$$

where ΔU is the decrease in internal elastic energy due to bulking and β is the fraction of the internal elastic energy converted to potential internal energy. The decrease in internal elastic energy is given by:

$$\Delta U = U_{D(t)} - U_{D(t+\Delta t)} \quad (11)$$

where

$$U_{D(t)} = \frac{\sigma^2}{6G} \quad (12)$$

The parameters σ and G appearing in Eq. (12) are the actual yield strength and the shear modulus of the damage-free ceramic material, respectively.

Strength Model

The most commonly used strength model for structural ceramics is the Johnson-Holmquist 2 (JH2) strength model [16]. The JH2 strength model is an empirical model capable of representing the material behavior displayed under high deformation rate, high-pressure and tensile hydrostatic pressure conditions, of the type encountered in problems dealing with ballistic impact and penetration conditions in ceramics. Within the JH2 strength model, the normalized yield (shear) strength is defined as:

$$\sigma^* = \sigma_i^* - D(\sigma_i^* - \sigma_f^*) \quad (13)$$

where σ_i^* is the yield strength of the intact (damage-free) ceramic, σ_f^* the yield strength of the fractured (damaged) ceramic and D the extent of damage.

The normalized yield strength, σ^*, is defined as:

$$\sigma^* = \frac{\sigma}{\sigma_{HEL}} \quad (14)$$

where σ is the actual yield strength and σ_{HEL} is the yield strength at the Hugoniot Elastic Limit (HEL). The normalized yield strengths σ_i^* and σ_f^* are also defined in a similar manner. The normalized yield strength of the intact ceramic material, σ_i, is given by:

$$\sigma_i^* = A(P^* + T^*)^N (1 + C \ln \dot{\varepsilon}^*) \quad (15)$$

and the normalized yield strength of the fractured ceramic is given by:

$$\sigma_f^* = B(P^*)^M (1 + C \ln \dot{\varepsilon}^*) \quad (16)$$

where A, B, C, M, N and T appearing in Eqs. (15) and (16) are all material specific constants while P^* and T^* are respectively defined as:

$$P^* = \frac{P}{P_{HEL}} \quad (17)$$

and

$$T^* = \frac{T}{P_{HEL}} \quad (18)$$

where P and T are the actual pressure and the maximum hydrostatic tensile pressure that the ceramic material can withstand, respectively, and P_{HEL} is the pressure at the Hugoniot Elastic Limit. The dimensionless material strain rate, $\dot{\varepsilon}^*$, appearing in Eqs. (17) and (18) is defined as:

$$\dot{\varepsilon}^* = \frac{\dot{\varepsilon}}{\dot{\varepsilon}_0} \tag{19}$$

where $\dot{\varepsilon}$ is the actual strain rate and $\dot{\varepsilon}_0$ is the reference strain rate (= 1.0 s^{-1}).

Failure Model

The most commonly used failure model for structural ceramics is the Johnson-Holmquist 2 (JH2) failure model [16] according to which the damage which leads to fracture of a ceramic is accumulated as:

$$D = \sum \frac{\Delta\varepsilon_p}{\varepsilon_p^f} \tag{20}$$

where $\Delta\varepsilon_p$ is the increment in effective plastic strain with an increment in loading and the failure strain ε_p^f is the plastic strain to fracture under a constant pressure P. The expression for the plastic strain at fracture is given by:

$$\varepsilon_p^f = D_1 (P^* + T^*)^{D_2} \tag{21}$$

where D_1 and D_2 are material specific constants and P^* and T^* are as explained in the previous section and fracture occurs when $D=1$, and, when the material loses its ability to support any tensile hydrostatic or deviatoric stress.

Erosion Model

The same erosion model was used as in the case of composite laminates.

2.2.3 Metallic Materials

Equation of State

For metallic materials (lead, tungsten and copper), the linear equation of state is used which assumes a Hooke's law type relationship between the pressure and the volume change $\mu = \left(\dfrac{\rho}{\rho_0} - 1\right)$ as:

$$P = K\mu \tag{22}$$

where K is the bulk modulus of the material.

Strength Model

To represent the constitutive response of metallic materials under deviatoric stress, the Johnson-Cook model [15] is used. This model is capable of representing the material behavior displayed under large-strain, high deformation rate, high-temperature conditions, of the type encountered in problems dealing with hypervelocity impact and

penetration conditions. Within the Johnson-Cook model, the yield stress is defined as:

$$Y = \left[A_1 + B_1 \varepsilon_{pl}^n\right]\left[1 + C_1 \log \dot{\varepsilon}_{pl}\right]\left[1 - T_{H0}^m\right] \tag{23}$$

where ε_{pl} is the equivalent plastic strain, $\dot{\varepsilon}_{pl}$ the equivalent plastic strain rate, A_1 the zero plastic strain, unit plastic strain rate, room temperature yield stress, B_1 the strain hardening constant, n the strain hardening exponent, C_1 the strain rate constant, m the thermal softening exponent and $T_{H0} = (T - T_{room})/(T_{melt} - T_{room})$ a room temperature (T_{room}) based homologous temperature while T_{melt} is the melting temperature. All temperatures are given in Kelvin.

Failure Model

For metallic materials which fail predominantly in a ductile mode, as is the present case, the failure condition is defined most frequently using the Johnson-Cook failure model [15]. The progress of failure according to the Johnson-Cook failure model is defined by the following cumulative damage law:

$$D = \sum \frac{\Delta \varepsilon}{\varepsilon_f} \tag{24}$$

where $\Delta \varepsilon$ is the increment in effective plastic strain with an increment in loading and ε_f, is the failure strain at the current state of loading which is a function of the mean stress, the effective stress, the strain rate and the homologous temperature, given by:

$$\varepsilon_f = \left[D_3 + D_4 \exp(D_5 \sigma^*)\right]\left[1 + D_6 \ln \dot{\varepsilon}_{pl}\right]\left[1 + D_7 T_{H0}\right] \tag{25}$$

where σ^* is mean stress normalized by the effective stress. The parameters D_3, D_4, D_5, D_6 and D_7 are all material specific constants. Failure is assumed to occur when $D=1$.

Erosion Model

The same erosion model was used as in the case of composite laminates.

2.3. Problem Definition and Computational Analysis

In the present work, a transient non-linear dynamics analysis of the impact and penetration of the all HJ1-composite and the Al_2O_3 hard-faced HJ1-based hybrid armor panels with non-AP and AP projectiles is carried out in order to determine the role played by different constituents in the ballistic performance of the armor. The work was limited to the case of a normal impact of the armor by the projectiles and, due to the axisymmetric nature of the problem; all the calculations are carried out using a two-dimensional (axisymmetric) model. A simple schematic of the projectile/armor impact/penetration problem analyzed here is given in Fig.3.

The areal densities of the all HJ1-composite armor and of the alumina and the HJ1-composite layers in the hybrid armor panels are selected to match the ones used in Ref. [2], so that a direct comparison can be made between the model predictions and the experimental results. In the case of the hybrid armor, the overall areal density was kept fixed at 51 kg/m^2.

Both the M80 FMJ non-AP projectile and the M2 AP projectiles were modeled as

cylindrical projectiles with a diameter of 7.32mm and a pointed conical tip. Both types of projectiles were fully jacketed with a 1mm thick copper casing. The core of the projectile was filled with lead in the case of the M80 FMJ non-AP projectile and tungsten in the case of the M2 AP projectile. The masses of the two projectiles (9.7g and 10.8g, respectively) were chosen to match the masses of the real projectiles.
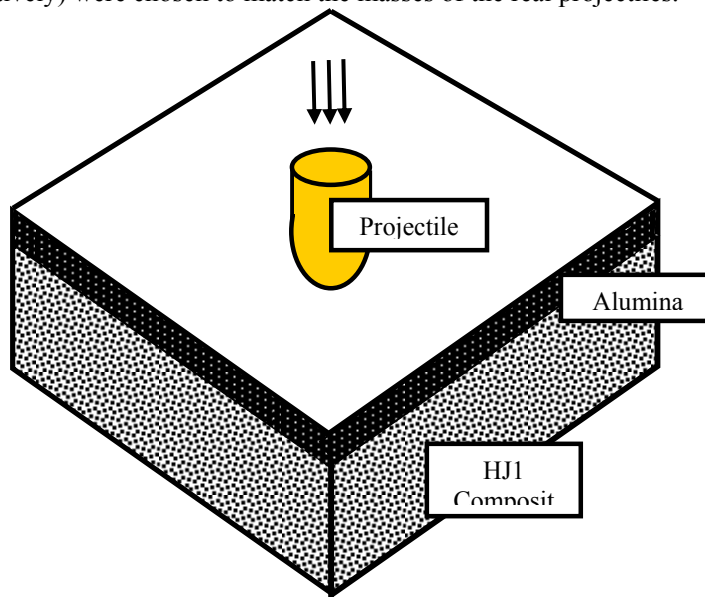

Fig.3. A schematic of the projectile/armor impact analyzed in the present work.

Two separate sets of analyses were carried out. In the first set, the all-composite and the ceramic-composite hybrid armors were modeled using the grid-based Lagrange processor while in the other set the gridless SPH processor was employed. In both cases, however, the projectile was analyzed using the Lagrange processor since the current version of AUTODYN allows the use of the SPH processors only for the computational domains with simple (rectangular, circular, etc.) geometry. The projectile domains were discretized using a mesh consisting of 200 rectangular cells. In the case of the SPH processor, the armor was represented by 32,100 interpolation particles. Conversely, a mesh consisting of 2100 rectangular cells was used when the armor was analyzed using the Lagrange processor. To improve the accuracy of the analysis, smaller cells were used in the regions of the projectile and the armor involved in the projectile/armor interactions. An example of the computational sub-domains used is shown in Fig.4. A standard mesh sensitivity analysis has been carried out in order to ensure that the results obtained are insensitive to the size change of the cells used. Similar approach was taken in the case of the SPH processor with respect to the size of the interpolation particles. A majority of the results presented in the next section were obtained using the SPH processor for the armor. The remaining results obtained through the use of the Lagrange processor for the armor are presented for the sole purpose of demonstrating the effect of processor choice on the computed results.

At the beginning of each calculation, a constant initial normal velocity is assigned to the projectile while the armor is kept at rest. Except for the projectile/armor contact

surfaces, zero-stress boundary conditions are prescribed on all faces of the projectile and the armor. Projectile/armor interactions were modeled using the AUTODYN sub-domain coupling option.
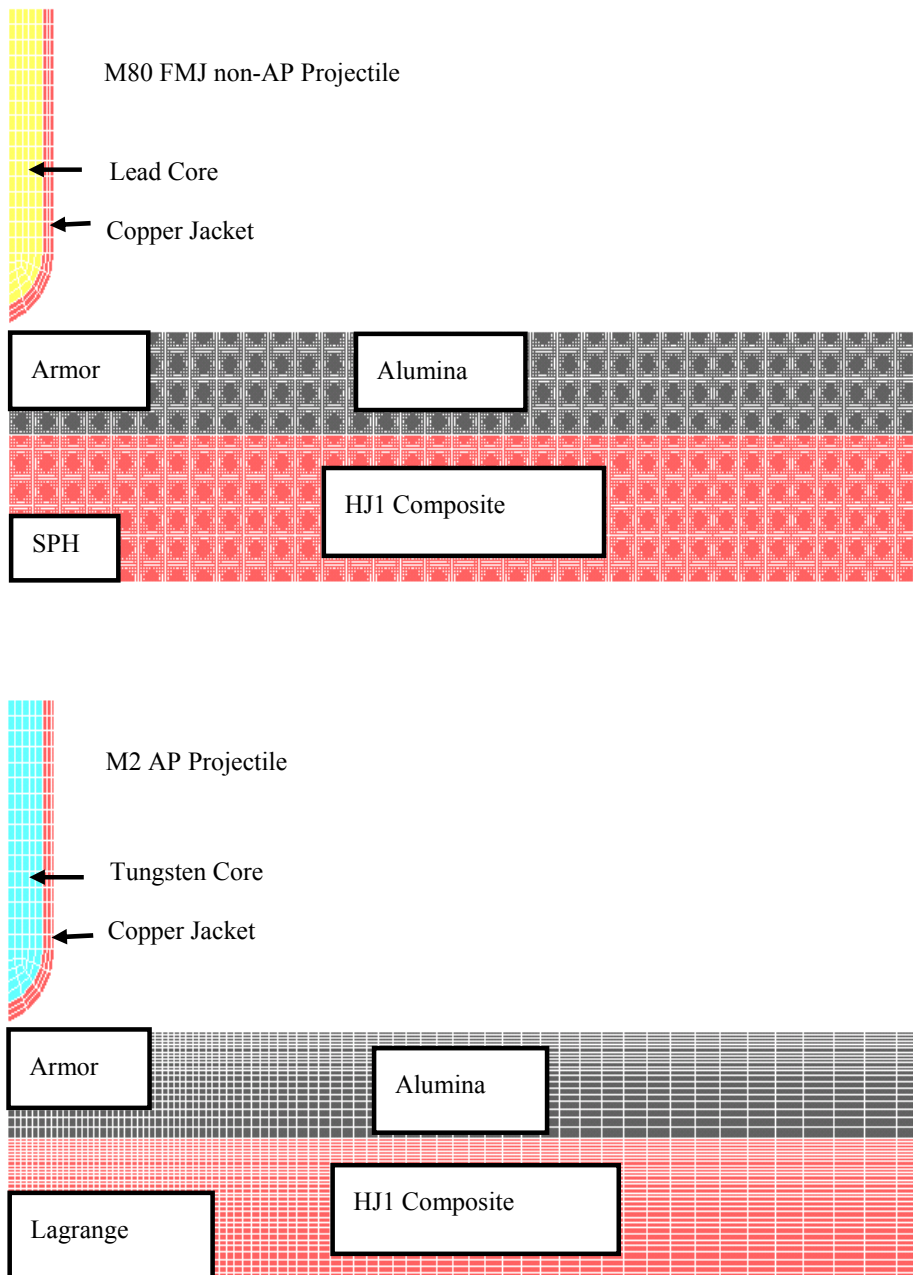

M80 FMJ non-AP Projectile

Lead Core

Copper Jacket

Armor

Alumina

HJ1 Composite

SPH

M2 AP Projectile

Tungsten Core

Copper Jacket

Armor

Alumina

HJ1 Composite

Lagrange

Fig.4. Computational domains used in the present work. Domains are not drawn to scale.

3. RESULTS AND DISCUSSION

3.1. Derivation and Validation of the Ballistic Materials Model for HJ1 Composite

The AUTODYN materials database does not contain a material model for the HJ1 composite but provides a model for a Kevlar Fiber Reinforced Polymer (KFRP) containing 53 vol. % of aramid fibers and an epoxy matrix. Since the objective of the present work does not include experimental determination of the materials model for the HJ1-composite, an effort was first made to modify the existing KFRP model so that it can be used to simulate the behavior of the HJ1-composite under the ballistic conditions. The modification of the KFRP model was done using the following procedure:

(a) It is first recognized that the composite-material elastic-stiffness constants, to the first order of approximation, scale with the axial Young's modulus of the constituent fibers and with the volume fraction of the fibers. In other words, the composite elastic stiffness properties are assumed to be controlled by the fiber stiffness properties. Consequently, the elements of the KFRP elastic-stiffness matrix are first multiplied by a ratio of the S-2 glass and aramid fibers Young's moduli and then by a ratio of the S-2 glass and aramid fibers volume fractions; and

(b) The yield surface behavior is assumed to be controlled by the yield behavior of the matrix and the volume fraction of the fibers. In other words, the onset and progression of plasticity is assumed to be controlled by the matrix yield stress modified by the (fiber volume fraction proportional) constraining effect of the rigid fibers. Consequently, the square root of the KFRP's R parameter appearing on the right hand side of Eq.(5) is modified by multiplying it first with a ratio of the cured phenolic resin and epoxy yield stresses and then with a ratio of the S-2 glass and aramid fibers volume fractions.

To test the validity of the resulting ballistic materials model for the HJ1-composite, the ballistic-performance V50 vs. areal density curve is first computed for the case of the .30 caliber M80 FMJ non-AP projectile. Next, the same procedure is repeated for the case of .30 caliber M2 AP projectile. Since, the computer simulations carried out here are of a deterministic nature (i.e. under given test conditions the projectile either passes or not through the armor panel), V50 is arbitrarily defined as the velocity at which the projectile penetrates the armor roughly half way.

A comparison of the V50 vs. areal density curves for the all-composite HJ1 armor test and the .30 caliber M80 FMJ non-AP and M2 AP projectiles obtained experimentally by Fecko et al. [2] and computationally in the present work is displayed in Fig.1. Overall, the agreement between the experimental and the computational results is satisfactory relative to both the absolute values of V50 and the rate of change of V50 with a change in the areal density. Based on this finding, it is deemed that the modified KFRP materials model can reasonably well account for the ballistic behavior of the HJ1 composite and can be used in the simulations of the penetration behavior of the ceramic hard-faced/composite-backing hybrid armor. As far as the ballistic behavior of alumina and the metallic materials in the projectiles are concerned, their models are taken directly from the AUTODYN materials database [8].

The temporal evolutions of the penetration of the all-composite HJ1 armor with an areal density of 52.5 kg/m^2 by an M80 FMJ non-AP projectile with an initial velocity of

950 m/s is displayed in Figs 5(a)-(c). The results displayed in Figs 5(a)-(c) can be summarized as follows:

(a) In addition to causing the formation of a penetration crater in the composite armor the non-AP projectile gives rise to a substantial damage in the armor in the regions surrounding the projectile;

(b) The main damage modes observed in the armor are: (i) bulk failure (denoted by blue color) located just below the crater; (ii) delamination (denoted by yellow-color mainly horizontal stripes) situated mainly in the region surrounding the crater; and (iii) fiber fracture (shown in grey color) found mainly in the vicinity of the projectile;

(c) The projectile has undergone a substantial amount of plastic deformation and erosion due to the low strength levels of the copper jacket and the lead core; and

(d) The observed damage modes in the armor and the deformation modes in the projectile are generally consistent with the *postmortem* experimental investigations of the armor and the projectile carried out by Fecko et al. [2].

3.2. Ballistic Performance of Ceramic/Composite Hybrid Armor

The transient non-linear dynamics analysis described in Section 2.3 is carried out in the present section in conjunction with the modified KFRP materials model for the HJ1 described in Section 3.1 to study the ballistic performance of a hybrid composite armor consisting of an HJ1-composite backing and an alumina hard-face. Since the computational results to be obtained are intended to be compared with their experimental counterparts reported by Fecko et al. [2], the overall areal density of the hybrid composite is kept constant and equal to $51kg/m^2$. For the same reason, only the ballistic performance of the hybrid armor (including a pure alumina armor) with respect to the M2 AP projectile was investigated.

A comparison of the V50 vs. the HJ1 content results for the alumina hard-face/HJ1-composite backing armor at a constant overall areal density of $51kg/m^2$ and with respect to the .30 caliber M2 AP projectile obtained experimentally by Fecko et al. [2] and computationally in the present work is displayed in Fig.2. The results displayed in Fig.2 can be summarized as follows:

(a) The overall agreement between the experimental and computational results is quite good over the entire range of the HJ1 contents;

(b) While the available experimental results suggest the existence of an optimal HJ1 content in a range between 0 and 40%, the computational results define this optimal HJ1 content more precisely placing it near 30%; and

(c) The linear relationship between V50 and the HJ1 content at the HJ1 contents exceeding 40% is reproduced by the computational results although the slope is somewhat different.

To better understand the role of the ceramic hard-face and the composite backing layers in the overall ballistic performance of the hybrid armor and to explain the existence of an optimal composite content, the transient non-linear dynamics analysis described in Section 2.3 is further used, in conjunction with the modified KFRP materials model for the HJ1, to monitor the evolution of the shape of AP projectile tip during its interactions with the two layers of the armor, changes in the projectile velocity and the temporal evolution of the pressure and material deformation/failure status within the two layers of the armor. Examples of the results obtained in this portion of the work

are given in Figs 6(a)-(c) and 7(a)-(c). It should be noted that the results displayed in Figs 6(a)-(c) pertain to the pure alumina armor while the ones displayed in Figs 7(a)-(c) pertain to the hybrid alumina/HJ1 composite armor with an optimal (30 %) content of the HJ1 composite backing.

The results displayed in Figs 6(a)-(c) can be summarized as follows:

(a) At the early stages of impact, Fig.6 (a), the pressure field in the all-alumina armor is dominated by a shock/impulse wave emanating radially from the point of impact. Concurrently the material deformation/failure status is dominated by the elastic and plastic deformations and crumbling of the alumina layer while the projectile undergoes a minor plastic blunting/erosion of its tip;

(b) At the intermediate stages of the impact, Fig.6 (b), when the shock/impulse wave begins to reflect from the back face of the armor a negative-pressure region is created at the back face of the armor. Due to a very low ability of alumina to support tensile loads, the material subjected to the negative pressure undergoes a brittle tensile failure. The projectile's tip blunting observed in (a) has continued giving rise to a significant erosion of the projectile's mass; and

In the late stages of the impact preceding the arrest of the projectile by the armor, Fig.6(c), the pressure field contains enlarged regions of both the positive pressure (armor regions surrounding the projectiles tip) and the negative pressure (regions near the armor's back face). Consequently, a larger volume of the armor has suffered structural damage through either crumbling (caused by the positive pressure) and/or tensile failure (caused by the negative pressure). Previously noted erosion of the projectile has continued.

The results displayed in Figs 7(a)-(c) can be summarized as follows:

(a) At the early stages of the impact, Fig.7 (a), the mechanical response of the hybrid armor and of the projectile is controlled by the alumina hard-face layer of the armor. Consequently, the results displayed in Fig.7(a) are quite similar to those displayed in Fig.6(a);

(b) At the intermediate stages of the impact, Fig.7 (b), when the shock/impulse wave reaches the alumina/HJ1-composite interface, a negative-pressure region begins to develop at the back face of the alumina layer. This gives rise to the onset of tensile failure of alumina in this region. As in the case of pure-alumina armor, the projectile experiences a substantial amount of plastic deformation and erosion, although the extent is somewhat lower than in the case of pure alumina armor; and

(c) At the later stages of the impact, Fig.7(c), when the projectile has already entered the HJ1-composite backing layer, a substantially larger region of alumina has been subjected to negative pressures and, consequently, has failed structurally. Meanwhile high pressures are observed in the HJ1-composite region surrounding the tip of the projectile. Due to high levels of the failure strength of the HJ1-composite high pressures do not give rise to a significant amount of damage. At the back face of the HJ1-composite layer, a small region subjected to negative pressure is observed. Composite failure in this region appears to be dominated by the fiber-failure mechanism. While the erosion-induced blunting of the projectile tip has continued, the extent of this blunting is clearly lower relative to the one observed in the case of the all-alumina armor, Fig.6(c).
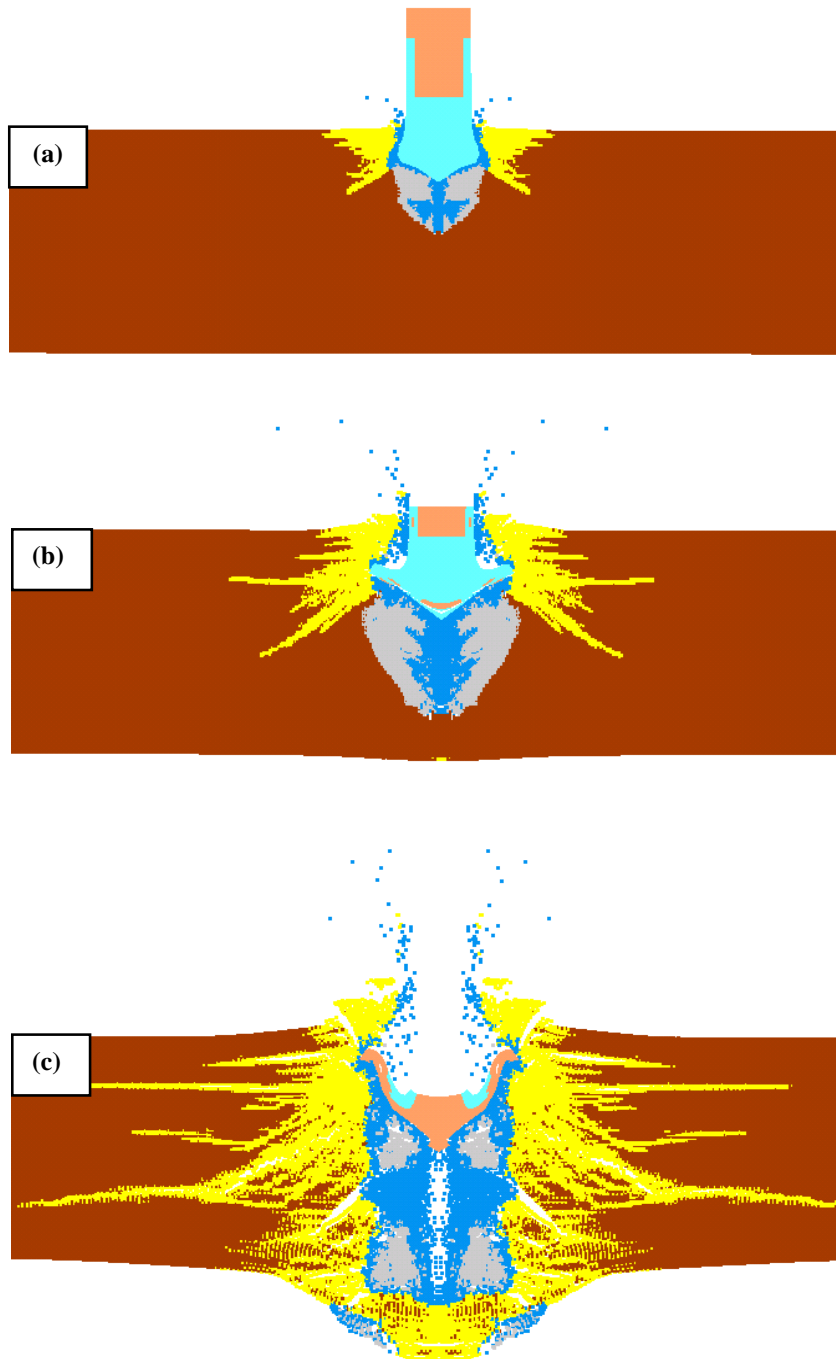
Fig.5. Temporal evolution of the penetration of HJ1 composite armor
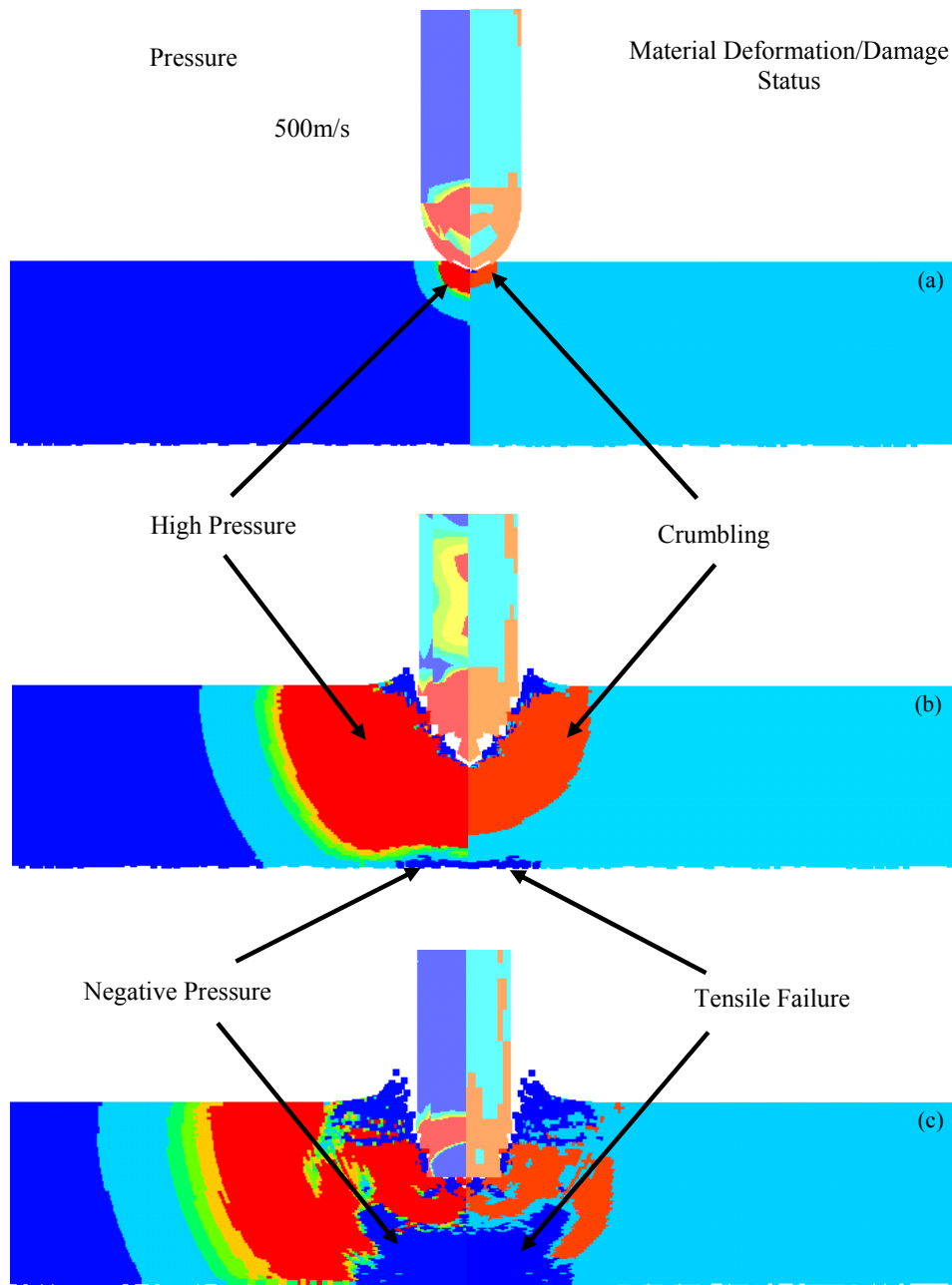by M80 FMJ non-AP projectile.

Pressure

Material Deformation/Damage
Status

500m/s

(a)

High Pressure

Crumbling

(b)

Negative Pressure

Tensile Failure

(c)

Fig.6. Temporal evolution of pressure (left side) and material deformation/damage status (right side) in an all-Al$_2$O$_3$ armor with an areal density of 51 kg/m^2.
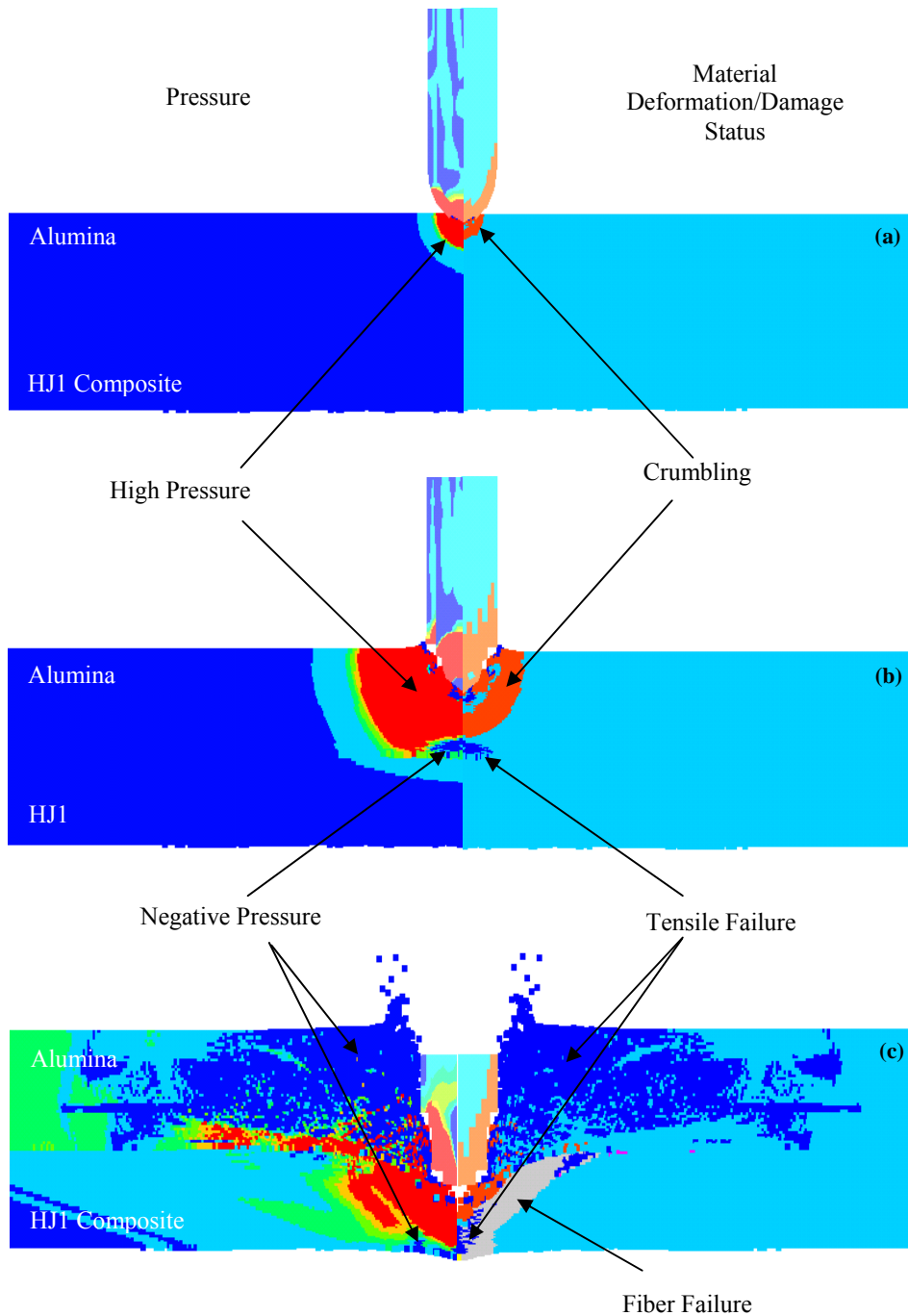
Fig.7. Temporal evolutions of pressure (left side) and material deformation/damage status (right side) in an Al_2O_3-hard face/ HJ1-composite armor with a HJ1-compostie content of 30% and with a total areal density of 51 kg/m^2.

To better understand the existence of an optimum HJ1 content with respect to the ballistic performance of the alumina/HJ1-composite hybrid armor as displayed in Fig. 2, the temporal evolutions of the projectile's mass and velocity is monitored for the hybrid armor containing 10%, 30% (the optimum HJ1 content) and 50% HJ1 content. It should be noted that a half of the product of the projectile's mass and the square of its velocity represents the kinetic energy of the projectile. Thus by monitoring the evolution of the projectile's mass and its velocity, it is possible to analyze the effectiveness of each armor in hand at eroding the projectile and capturing its kinetic energy. It should be noted that the erosion mechanism applied to the Lagrange domain occupied by the projectile is a mathematical tool used to prevent numerical difficulties associated with highly distorted Langrange cells. Nevertheless, since excessive deformation is a basis for a number of wear/erosion mechanisms (e.g. [17]), the erosion algorithm used in this paper is treated as an algorithm accounting for the physical wear of the projectile accompanying its excessive deformation. The effect of the choice of the erosion strain magnitude on the computational results is discussed in the next section.

Temporal evolutions of the AP projectile's mass and velocity in the three hybrid armors are shown respectively in Figs 8(a)-(b). Filled circles are used in Fig. 8(a) to indicate the approximate time of entry of the projectile into the HJ1-composite backing. The results displayed in Figs 8(a)-(b) can be summarized as follows:

(a) Alumina hard-face is primarily responsible for erosion of the projectile and blunting of its tip as represented by decrease in the projectile's mass, Fig.8(a);

(b) The HJ1-composite backing is mainly responsible for capturing the projectile's kinetic energy as represented by the projectile's velocity, Fig.8(b); and

(c) The optimal HJ1-composite content corresponds to the case where there is an optimal combination of the alumina's contribution to erode and blunt the projectile and the HJ1-composite's ability to absorb the projectile's kinetic energy. When the alumina content is too small, the projectile remains pointed and retains most of its mass and velocity, so that the behavior of the hybrid armor resembles that of a pure HJ1-composite armor. Conversely, when the HJ1-composite content is not sufficient the projectile undergoes a substantial amount of blunting and erosion. However, the velocity of the projectile remains high so that the insufficiently-thick HJ1-composite backing is not capable of fully absorbing its kinetic energy before a complete armor penetration takes place.

3.3. Choice of the Processor

All the results presented thus far were obtained using the meshless SPH processor for the all-composite and the ceramic/composite hybrid armor. As mentioned earlier, the current version of AUTODYN allows only computational domains with simple geometries (rectangular, circular, etc.) to be modeled using the SPH processor. For that reason, the non-AP and AP projectiles were represented using only the Lagrange processor. As pointed out earlier, the size of the mesh in the case of the Lagrange processor and the size of the interpolation particles in the case of the SPH processor were selected in such a way that their further refinement does not measurably affect the computed results.
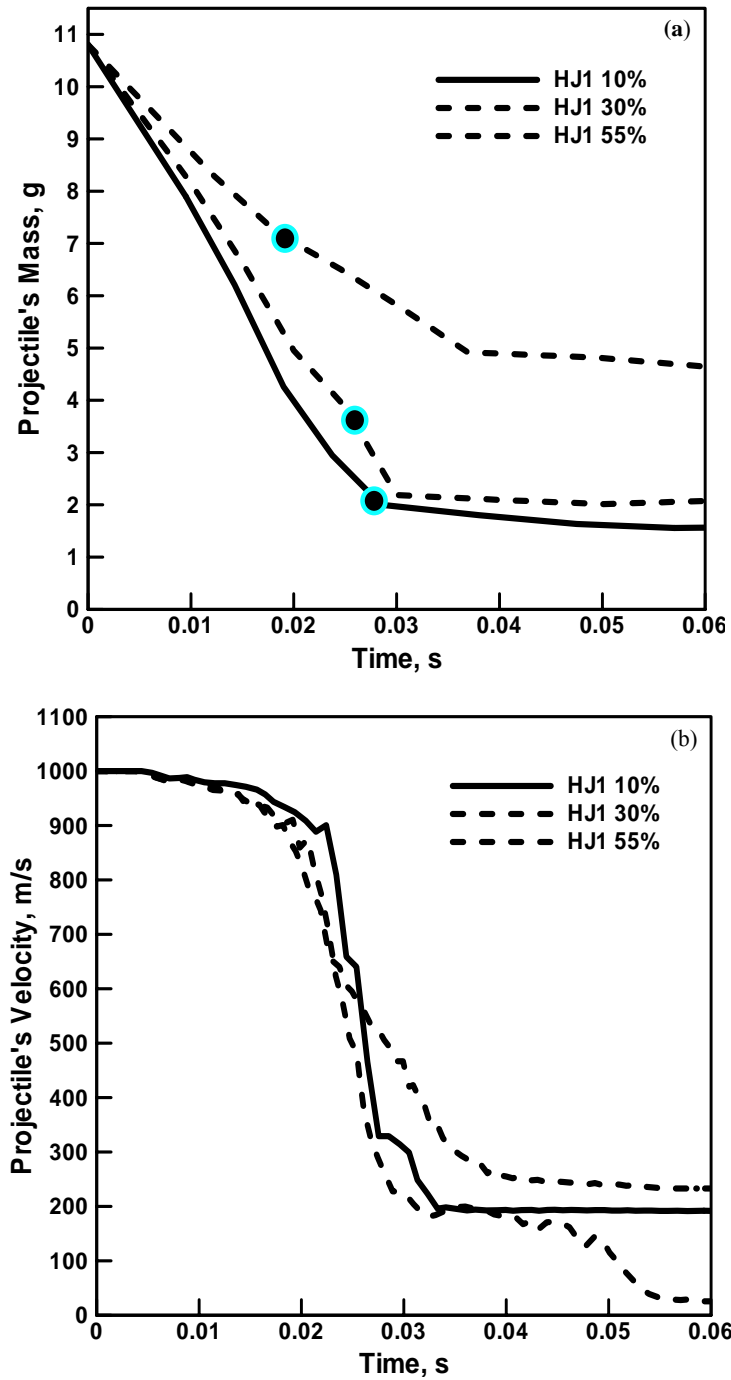
Fig.8. Temporal evolutions of **(a)** projectile's mass and **(b)** projectile's velocity for the Al$_2$O$_3$-hard face/ HJ1-composite armors with 10%, 30% and 55% HJ1-composite content.

The ballistic performance of the all-composite and the hybrid types of ceramic/composite armor presented in the previous two sections is also analyzed using the Lagrange processor. It was found that the computed results obtained using the Lagrange processors are significantly dependent on the choice of the magnitude of erosion strain. As shown in Fig.9, if the erosion strain is properly selected, a reasonably good agreement can be obtained between the corresponding computed results obtained using the SPH processor (Fig.9(a)) and the results obtained using the Lagrange processor (Fig.9(b)). However, a substantially different computed result can be obtained using the Lagrange processor with a different choice of erosion strain (Fig.9(c)). Again, it should be noted that the mesh size was chosen in such a way that its further refinement does not significantly affect the computed results, i.e., the observed differences between the results shown in Figs 9(b) and 9(c) are solely caused by the selection of magnitude of the erosion strain. Since there are no general guidelines for the selection of magnitude of the erosion strain, the SPH processor appears to be a preferred computational approach for analysis of the ballistic performance of the composite and hybrid armor structures.
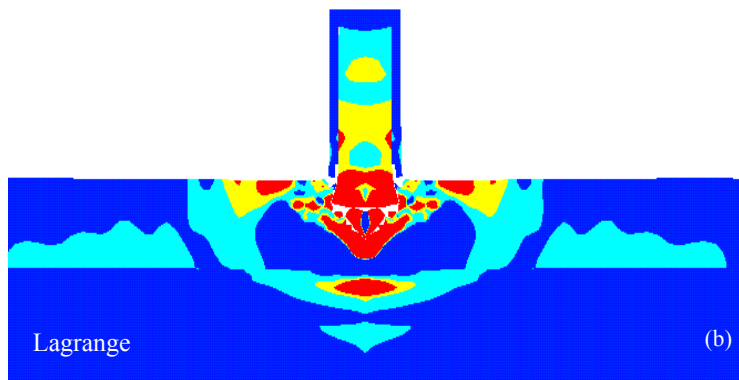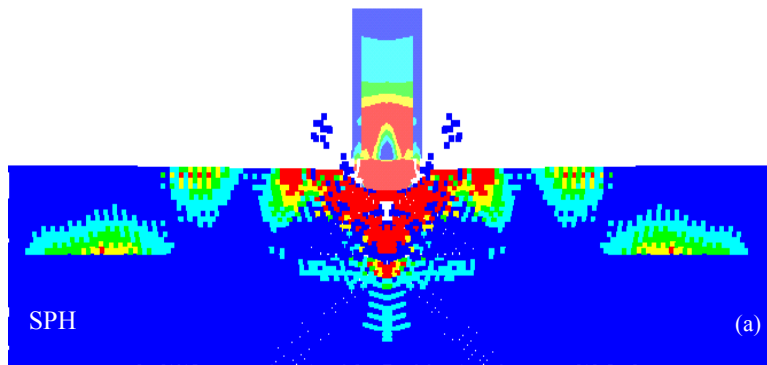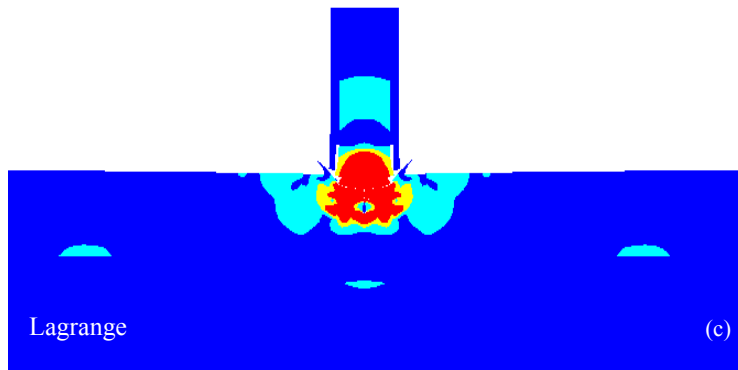
Fig.9. A comparison of the pressure fields obtained using: **(a)** the SPH processor and **(b)** and **(c)** the Lagrange processor with erosion strains of 1.5 and 0.5, respectively.

4. SUMMARY AND CONCLUSIONS

Based on the results obtained in the present work, the following main summary remarks and conclusions can be drawn:

1. By recognizing that the stiffness of a polymer matrix composite is primarily controlled by the stiffness of its fiber reinforcements and that its plastic yielding is controlled by the plasticity of its polymer matrix constrained by fiber reinforcements, the existing ballistic materials model an epoxy-matrix Kevlar Fiber-Reinforced polymer (KFRP) was successfully converted into the corresponding model for the HJ1-composite based on the S-2 glass fibers and a phenolic resin matrix.

2. The roles of alumina hard-face and a HJ1-composite backing in providing the necessary ballistic resistance of the alumina/HJ1-composite hybrid armor relative to the AP projectiles has been revealed through the use of a transient non-linear dynamics computational analysis of the armor penetration problem.

3. The optimal contents of the alumina hard-face and the HJ1-composite backing have been rationalized as an optimal contribution of the two armor constituents to eroding/blunting the projectile and capturing its kinetic energy.

Acknowledgements

REFERENCES

[1]. *U.S. Military Department of Defense Specification*, MIL-A-12560H95, July 1991.

[2]. D. Fecko, P. Douglas and D. Murray, The Synergistic Roles of High Strength Glass Composite and Alumina Ceramic Facing in Light Weight Composite Armor Against Armor Piercing Projectiles, *Technical Report, 2002*, Advanced Glassfiber Yarns LLC., 2558 Wagener Road, Aiken, SC, 29801.

[3]. D. R. Hartman, Ballistic Impact Behavior of High-Strength Glass-Fiber Composites, *41st Annual Conference*, Reinforced Plastics Institute, The Society of the Plastics Industry, Inc., Session 16-D, January 1986, 1-5.

[4]. S. J. Bless and D. R. Hartman, Ballistic Penetration of S-2 Glass Laminates, *21st SAMPE Technical Conference*, September 1989, 852-866.

[5]. S. J. Bless, M. Beyami and D. R. Hartman, Penetration through Glass Reinforced Phenolic, *22nd SAMPE Technical Conference*, November 1990, 293-303.

[6]. *Advanced Glass Fiber Yarns*, Ballistic Training Manual, Advanced Glass Fiber Yarns.LLC, Aiken, South Carolina, 2002.

[7]. J. Langford and W. Gray, *Composite Armor, in Concise Encyclopedia of Composite Materials*, Edited by A. Kelly, Pergamon Press, (1989)55-62.

[8]. *AUTODYN-2D and 3D*, Version 5.0, User Documentation, Century Dynamics Inc., 2004.

[9]. M. Grujicic, B. Pandurangan, K. L. Koudela and Bryan Cheeseman, A Computational Analysis of the Ballistic Performance of Light-Weight Hybrid-Composite Armor, *Applied Surface Science*, accepted for publication, January 2006.

[10]. R. A. Clegg, C. J. Hayhurst, J. G. Leahy and M. Deutekon, Application of a Coupled Anisotropic Material Model to High Velocity Impact Response of Composite Textile Armor, *18th International Symposium on Ballistics*, San Antonio, Texas, 15-19 November 1999, 791-798.

[11]. C. E. Anderson, P. A. Cox, G. R. Johnson and P. J. Maudlin, A Constitutive Formulation for Anisotropic Materials Suitable for Wave Propagation Computer programme-II, *Computational Mechanics*, 15(1994)201-223.

[12]. M. Grujicic, B. Pandurangan, C. L. Zhao, S. B. Biggers and D. R. Morgan, Hypervelocity Impact Resistance of Reinforced Carbon-Carbon/Carbon-Foam Thermal Protection Systems, *Applied Surface Science*, accepted for publication, July 2005.

[13]. E. Gruneisen, Handbuch der Physik, Springer-Verlag, Berlin, 10, 1926.

[14]. W. Riedel, D. M. White, R. A. Clegg and W. Harwick, *Advanced Material Damage Models for Numerical Simulation Codes*, EMI-Report No. I 75/03, ESA CR (P) 4379, October 2003.

[15]. G. R. Johnson and W. H. Cook, A Constitutive Model and Data for Metals Subjected to Large Strains, High Strain Rates and High Temperatures, *Proceedings of the 7th International Symposium on Ballistics*, 1983.

[16]. G. R. Johnson and T. J. Holmquist, An Improved Computational Constitutive Model for Brittle Materials, *High Pressure Science and Technology*, 1993. (AIP, New York, 1994).

[17]. B. K. Tanner, H. Z. Wu, S. G. Roberts and T. P. A. Hase, Subsurface damage in alumina and alumina–silicon carbide nanocomposites, *Phil. Mag.*, 84(12)(2004)1219-1232.